

KEK preprint 94-180
 NWU-HEP 95-01
 DPNU-95-02

Electron identification using the TOPAZ detector at TRISTAN *

Masako Iwasaki^{a†}, Eiichi Nakano^{b‡}, and Ryoji Enomoto^{c§}

^a*Department of Physics, Nara Women's University, Nara 630, Japan*

^b*Department of Physics, Nagoya University, Nagoya 164, Japan*

^c*National Laboratory for High Energy Physics, KEK, Ibaraki 305, Japan*

Abstract

We present an electron-identification method using the time-projection chamber and the lead-glass calorimeter in the TOPAZ detector system. Using this method we have achieved good electron identification against hadron backgrounds over a wide momentum range in the hadronic events produced by both single-photon exchange and two-photon processes. Pion-rejection factors and electron efficiencies were 163 and 68.4% for high- P_T electrons and 137 and 42.7% for low- P_T electrons in the single-photon-exchange process, and 8600 and 36.0% for the two-photon process, respectively.

1 Introduction

The TOPAZ detector is located at the TRISTAN e^+e^- collider of KEK. The center-of-mass energy was 58 GeV and the integrated luminosity will be more than 300pb^{-1} by the end of 1994.

Electron identification at high purity and high acceptance is necessary to tag heavy-quark events. In the e^+e^- annihilation process, the forward-backward asymmetry of quark-pair production becomes maximum at the TRISTAN energy region. A high-accuracy measurement of this was achieved [1, 2]. In two-photon processes, open-charm production was also studied with high accuracy [3]. Especially for low- P_T charm production, electron identification provides the best prove for resolved-photon processes [4], as well as for higher order corrections of the QCD [5].

In order to carry out these studies we need good electron identification over a wide momentum range. In particular, the detection of low-momentum electrons is necessary. To meet these requirements we have developed a method which uses an energy-loss measurement with a time-projection chamber and an energy measurement with a lead-glass calorimeter. In this article we present related details.

2 The TOPAZ detector system

The TOPAZ detector is a general-purpose 4π spectrometer featuring a time-projection chamber (TPC) as its central tracking device [6, 7, 8, 9]. A schematic view is shown in Figure 1. Charged tracks were

*submitted for publication.

†internet address: masako@kekvox.kek.jp

‡internet address: nakano@kekvox.kek.jp

§internet address: enomoto@kekvox.kek.jp

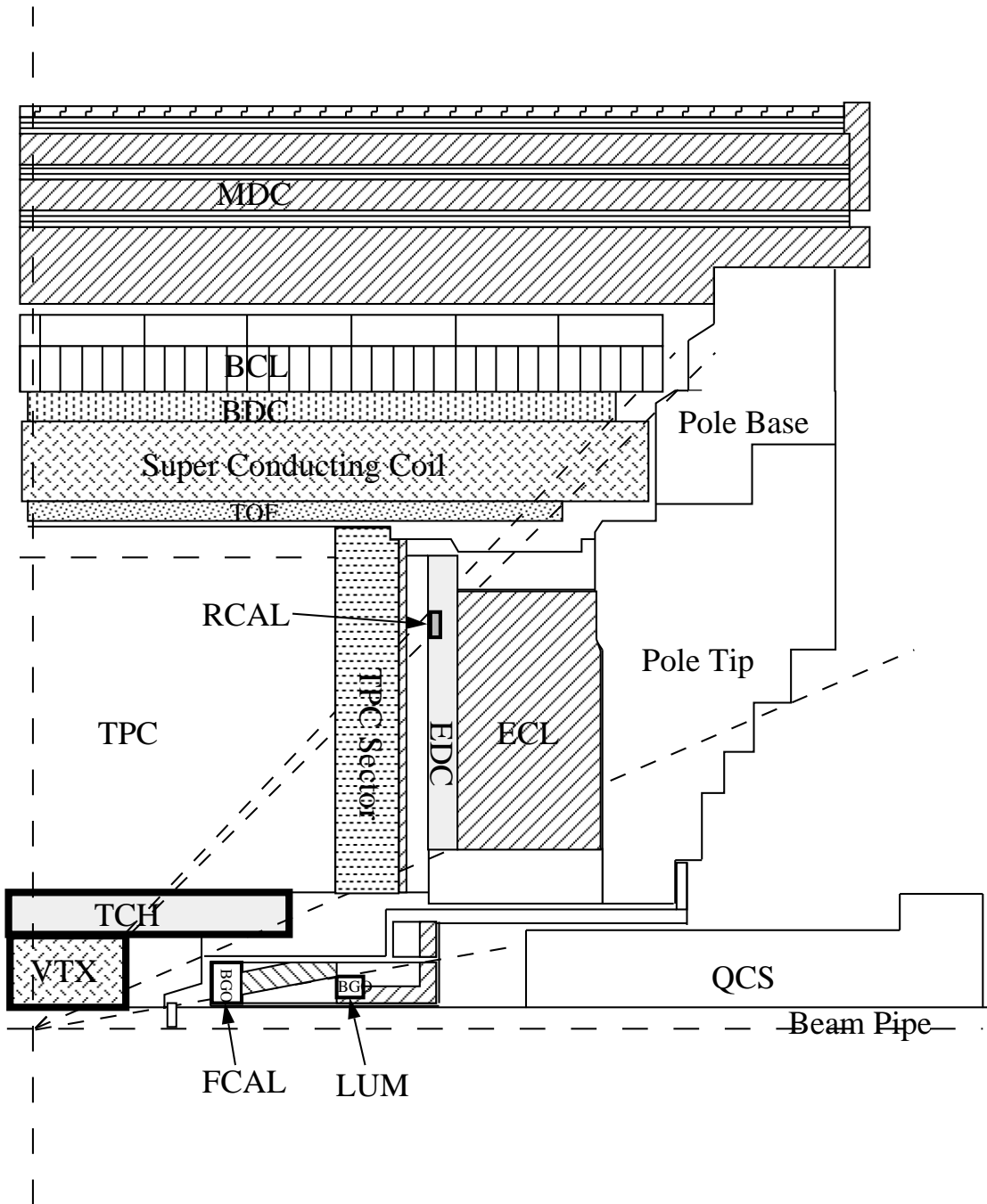


Figure 1: Schematic view of the TOPAZ detector.

Components	Material and size	Measured Performance
Magnet	2.9m ϕ \times 5m, 0.7 X_0	B=1.0 T
Beam pipe	10cm ϕ , 1mmt Be	
Vertex Chamber	Jet-chamber	$\sigma=40\mu\text{m}$
TCH	Cylindrical Drift Chamber	$\sigma=200\mu\text{m}$
TPC	2.4m ϕ \times 2.2m	$\sigma_{r\phi}=185\mu\text{m}$
	16 sectors	$\sigma_z=335\mu\text{m}$
	10 pad rows, 176 wires / sector	$\sigma_{dE/dx}=4.6\%$
	Ar/CH ₄ (90/10) 3.5atm	$\sigma_{P_T}/P_T = \sqrt{(1.5P_T)^2 + 1.6^2}\%$
TOF	Plastic Scintillator	$\sigma=220\text{ps}$
BDC	Streamer tube	$\sigma=350\mu\text{m}$
BCL	Lead-glass (SF6W), 20 X_0	$\sigma_E/E = \sqrt{(8/\sqrt{E})^2 + 2.5^2}\%$
	4300 blocks	$\sigma_\theta=0.38^\circ$
	$ \cos\theta \leq 0.82$	
ECL	Pb-PWC sandwich	$\sigma_E/E = 6.7\%$
	18 X_0	(for 26-GeV electron)
	$0.85 \geq \cos\theta \leq 0.98$	$\sigma_\theta=0.7^\circ$

Table 1: Performance of the TOPAZ detector components.

detected with the TPC placed in an axial magnetic field of 1.0 tesla. The energies of the photons and electrons were measured using a barrel lead-glass calorimeter (BCL) and an end-cap Pb-PWC sandwich calorimeter (ECL). A summary of the TOPAZ detector is given in Table 1. The coordinate system used in this article is as follows: z is defined as the beam-electron direction; x is the vertical axis and y is the horizontal axis. The major components of the TOPAZ detector are described in the following sections.

2.1 The Time-Projection Chamber (TPC)

The Time-Projection Chamber (TPC) is a three-dimensional tracking chamber which can identify particle species by energy-loss measurements. It has a fiducial volume of 2.4m in diameter and 2.2m in axial length, comprises 16 multiwire proportional counters (sectors), each equipped with 175 sense wires and 10 rows of segmented cathode pads, and is filled with a gas mixture of 90% Ar and 10% CH₄ at 3.5 atm [6].

Charged particles passing through the TPC sensitive region ionize gas molecules and liberate electrons along their trajectories. These electrons drift along the direction of the electric field toward the sectors at a speed of 5.3 cm/ μsec , and finally produce avalanches around sense wires; induced signals are detected by cathode pads. In order to reduce any space-charge effects, the gating-grid plane is placed above the shielding-grid plane. The signals from wires and pads are amplified and are shaped by analogue electronics. They are then fed into charge coupled device (CCD) digitizers sampling the wave-forms in units of a 100nsec ‘‘bucket’’ from which the z-positions and energy-loss (dE/dx) information are extracted.

The spatial and momentum resolutions are studied with cosmic rays as well as Bhabha and $\mu^+\mu^-$ events. The spatial resolution was obtained to be $\sigma_{xy}=185\mu\text{m}$ and $\sigma_z=335\mu\text{m}$. The momentum resolution was obtained by comparing two measurements in the opposing sectors in cosmic-ray events to be

$$\sigma_{P_T}/P_T = \sqrt{(1.5P_T)^2 + 1.6^2}\%.$$

The dE/dx resolution was studied using minimum-ionizing pions in the beam events. The obtained resolution is $\sigma_{dE/dx}=4.6\%$ after calibration (discussed later).

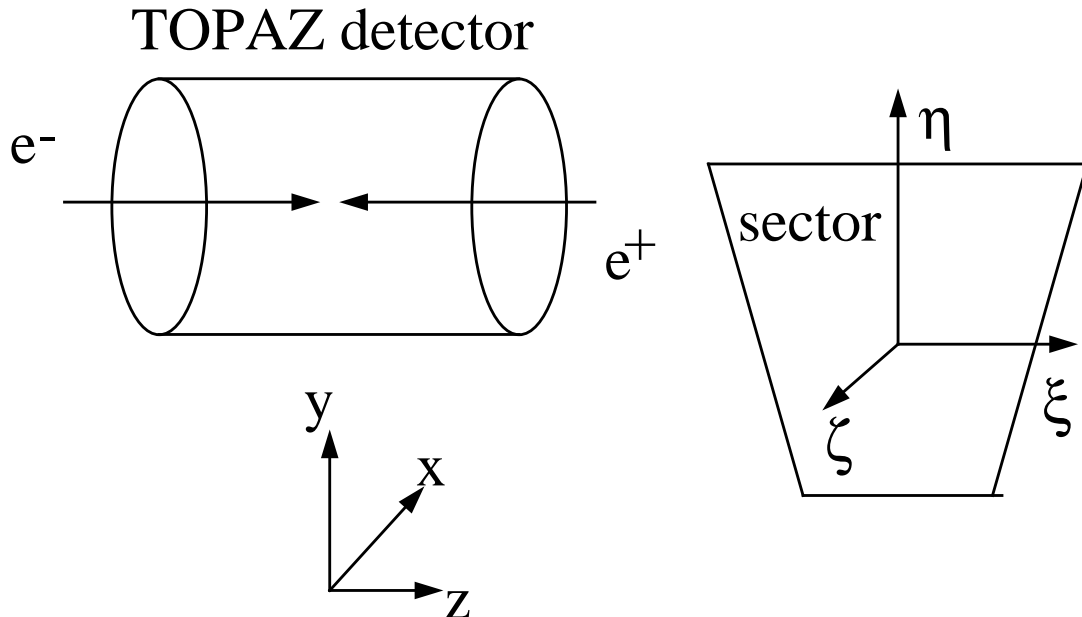


Figure 2: Definition of the coordinate system in the TOPAZ detector.

2.2 The Barrel Lead-Glass Calorimeter (BCL)

The Barrel Calorimeter (BCL), which comprises 4300 lead-glass Čerenkov counters, has a cylindrical structure covering an angular region of $|\cos\theta| \leq 0.82$. The calorimeter is divided into 72 modules, 8 in the ϕ direction and 9 in the z direction, each of which has an array of 60 lead-glass counters [7].

Each lead-glass counter is made of SF6W and has 20 radiation lengths, so that it can absorb more than 95% of the shower energies at TRISTAN's highest energy. The lead-glass blocks are tilted by 1.8° with respect to the radial line in the $r - \phi$ plane so that no photons coming from the interaction point escape through the counter-to-counter gaps. The Čerenkov light emitted in a lead-glass counter is detected by a photomultiplier after passing through a light guide. The signal from the photomultiplier is sent to a digitizer and is used for a neutral trigger [9]. The system is calibrated by using a Xe flash lamp.

The performance of the BCL has been studied by using Bhabha events. The energy and spatial resolution were determined to be $\sigma_E/E = \sqrt{(8/\sqrt{E})^2 + 2.5^2\%}$ and $\sigma_\theta = 0.38^\circ$, respectively.

3 Track reconstruction

The raw data was first corrected for any channel-to-channel variation of electronics. The spatial positions of “hits” in the TPC were then determined using pad signals, and particle tracks were searched among these points. Each found track was fitted to a helix, and the charge and momentum were assigned.

We define the coordinate system in the TOPAZ detector as shown in Figure 2. The global coordinate in the TOPAZ detector is defined by x , y and z . The origin of the coordinates is the detector center. The ξ , η and ζ are coordinates fixed on the TPC sector. The ξ -axis is along the sense-wire direction, the η -axis points in the radial direction at the center line of the sector, and the ζ -axis is along the beam line. The details concerning this section can be found in reference [10].

3.1 Space-point reconstruction

The pad signal of each channel was first corrected for any electronics variation, and was then examined as a function of the CCD bucket number. Contiguous signals were grouped into a cluster to form a ζ hit. The peak pulse height and the ζ position of the cluster were calculated by fitting the highest three CCD buckets to a parabola. Clusters were then searched in the ξ direction. If signals in contiguous pads had roughly the same ζ positions (within 1cm), these signals were combined into a cluster.

When a cluster was found, the ξ and η positions of the cluster were determined. Since the charge distribution along the pad row has approximately a Gaussian shape, the ξ position was calculated by fitting the highest 3 pad pulse heights to a Gaussian. If the cluster had only two pad signals, the pre-determined width of the Gaussian was used in the fit. The η position of the cluster was calculated by taking the centroid of the signals of five wires nearest to the pad row.

The position resolutions in ξ and ζ were studied using cosmic-ray tracks; typical values were obtained as $\sigma_\xi = 230\mu m$ and $\sigma_\zeta = 340\mu m$.

3.2 Track reconstruction

To find tracks from the reconstructed hits in the TPC, all found space points were first filled in a 2-dimensional histogram with ϕ and $z(R_{ref})$ axes such that

$$\begin{aligned}\phi &= \tan^{-1}(x/\sqrt{x^2 + y^2}) \\ z(R_{ref}) &= z \times (R_{ref}/R),\end{aligned}$$

where R_{ref} is the radial position of the fixed reference point. The space points associated to a track from the origin with a relatively high momentum were clusterized in a bin of the histogram. The track finding began by searching for a bin containing more space points than a given threshold. The threshold was set at 9 in the beginning, which corresponded to 10 pad row hits; it was then lowered by one when all of the bins above the current threshold were found. Lowering of the threshold was repeated until the threshold became two (three pad rows).

To test whether the space points in the bin formed a track or not, three space points which spanned the largest lever arm were chosen and checked as to whether they were on a single helix. If the space points were on a helix, other space points in the bin were checked as to whether they were consistent with the helix. If not, another set of three space points were chosen and the test was repeated. If a sufficient number of space points could be associated they were recognized to form a track and were fitted to a helix function.

Before the helix fitting, the space points were corrected for any dependence on the track angle to the sectors. The helix function was parametrized as follows:

$$\begin{aligned}x &= \frac{1}{\kappa}(\cos\phi_0 - \cos(\phi + \phi_0)) + d_r \cos\phi_0 + X_0 \\ y &= \frac{1}{\kappa}(\sin\phi_0 - \sin(\phi + \phi_0)) + d_r \sin\phi_0 + Y_0\end{aligned}$$

and

$$z = -\left(\frac{1}{\kappa}\right)\phi \tan\lambda + d_z + Z_0,$$

where

(X_0, Y_0, Z_0) is the position of the pivot,

κ is the inverse of the radius of the helix,

ϕ_0 is the angle of the pivot to the x axis,

d_r and d_z are the distance of the pivot from the true trajectory, and

λ is the the angle which the track makes with the xy plane.

The parameters to be determined by the fit are

$$d_r, \phi_0, \kappa, d_z, \text{ and } \tan\lambda.$$

The fitting of the helix was achieved by minimizing χ^2 defined as

$$\chi^2 = \sum_i \left(\left(\frac{\xi_i - \xi(\eta_i)}{\sigma_{\eta_i}} \right)^2 + \left(\frac{z_i - z(\eta_i)}{\sigma_{z_i}} \right)^2 \right),$$

where ξ_i and z_i are the measured position in the i 'th pad row and $\xi(\eta_i)$ and $z(\eta_i)$ are the expected position by the helix. We checked this χ^2 and made a final decision as to whether to recognize the space points as a track or not.

After all histogram bins forming tracks were found, the space points which were not recognized as tracks were then examined. From the remaining histogram bins, the bin containing the largest number of space points was searched for. The inner-most space point in the bin was chosen to be the origin (pivot) of the new histogram. The new histogram was defined with wider bins so that the space points of a low-momentum track could be clustered in a bin as a new track candidate. The bins were tested in the same way as described above.

3.3 Track Refinement

Although the gating grid prevents the feed-back of positive ions into the drift space and reduces the distortion in the electric field in the TPC, a small amount of distortion still remains, resulting in a systematic shift in the space-point determination. The dielectric material in the TPC, such as field cages, are also a source of distortion.

In addition to electrostatic distortion, the spatial positions of the TPC sectors may deviate from the designed position. This also causes a shift in the determination of the space points.

The electrostatic distortions in the $r\phi$ plane were parametrized as

$$\Delta x_\phi = a_0(r - r_{ref})^2,$$

where Δx_ϕ is the position displacement in ϕ due to the distortion. The deviations of the sector position in the $r\phi$ plane ($\Delta\zeta$, $\Delta\eta$) are parametrized as

$$\Delta\xi = d_\xi - \delta\eta$$

and

$$\Delta\eta = d_\eta + \delta\xi.$$

The shift in the z direction (dz) was expressed so as to include both the electrostatic distortion and the position displacements of the sectors, and was parametrized as

$$\Delta z = d_z + d_v z.$$

These parameters were defined for each sector. The parameters of the electrostatic distortions were determined based on a comparison of two cosmic-ray data taken when the beam was on and off. The parameters of the position displacements of the sectors and the shift in the z -direction were determined

based on a comparison of two measurements for a cosmic-ray track by two sectors when the beam was on. The space points calculated in the previous sections were corrected for any distortions using these parameters.

Finally, the space points were fitted to a helix again in order to assign the sign of the charge and momentum to the track. The momentum in the xy plane (P_T) and along the z -axis (P_L) were expressed using the helix parameters as

$$P_T = \left| \frac{Q}{\alpha\kappa} \right|$$

and

$$P_L = P_T \tan\lambda,$$

where

$$\alpha = \frac{1}{cB} = 333.56 \text{ cmGeV}^{-1}.$$

Q is the charge of the particle, c the velocity of light, and B the strength of the magnetic field (1.0 tesla). The sign of the charge was determined from the sign of κ .

The resolution of the momentum measurement was estimated using the cosmic rays [11]. The resolution was studied by comparing two measurements in opposite sectors for a cosmic-ray track. The momentum resolution was studied as a function of momentum, and was obtained as

$$\frac{\Delta P_T}{P_T} = \sqrt{[(1.5 \pm 0.1)P_T]^2 + (1.6 \pm 0.3)^2}\%.$$

The effect of distortion corrections was studied using Bhabha events. The momentum resolution for the Bhabha events was measured to be $(1.7 \pm 0.1)P_T\%$.

4 Energy-loss measurement in the TPC

The energy loss per unit length (dE/dx) is a function of the velocity (β) and the charge (Q) of a particle. In this section we examine the property of the dE/dx curve and discuss what determines the dE/dx resolution. In practice, the dE/dx resolution suffers from various systematic shifts due to temperature, pressure, high voltage, electronics and so on. We need to improve the resolution as much as possible in order to maximize the searchable region. A detailed description of the derivation of dE/dx is given here.

4.1 Theoretical consideration

4.1.1 Average energy loss

When a charged particle traverses a medium it interacts with atoms in the medium. The dominant process of energy loss is atomic excitation. The probability of exciting an atom scales as the square of the transverse component of the incident particle's electric field with respect to its velocity vector. The transition probability, and hence the energy loss, scales as the charge of the incident particle squared.

Qualitatively, the average energy loss ($\langle dE/dx \rangle$) in the material can be described as a function of the velocity (β) and charge (Q) of the particle. The function can be approximately written as

$$\langle \frac{dE}{dx} \rangle \approx \frac{4\pi n Q^2 e^2}{m_e e^2 \beta^2} \left(\ln \frac{2m_e \beta^2 \gamma^2}{I^2 + (\hbar\omega)^2 \beta^2 \gamma^2} - 2\beta^2 \right),$$

where

I is the logarithmic mean atomic ionization potential,

ω is the plasma frequency of the medium,

n is the electron density of the medium,

m_e is the electron mass,

e is the electron charge, and

Q is the charge of the incident particle.

The values of $\langle dE/dx \rangle$ fall as $1/\beta^2$ with increasing the momentum of the particles. The fall off is due to the fact that a particle traversing the material spends less time in the electric field of atoms, and, hence, transfers less energy as the particle's velocity increases. The ionization becomes minimum at $\beta\gamma \simeq 3$, and then $\langle dE/dx \rangle$ rises logarithmically as the momentum increases. This "relativistic rise" is the result of the relativistic increase in the transverse electric field of the incident particle. The $\langle dE/dx \rangle$ finally reached the plateau due to the "density effect" caused by the polarization of the medium.

4.1.2 Energy-loss distribution

There are two contributions to the shape of the energy-loss distribution: atomic excitations and δ - ray production. The δ - ray contribution falls inversely proportional to the energy-transfer squared ($1/(\Delta E)^2$), because this is the classical Rutherford scattering for free electrons. This process makes a long tail, called Landau tail, in the energy-loss distribution up to the kinematical limit. The peak of energy loss distribution is due to atomic excitation, which is the dominant energy-loss process. Argon, which is the main component of the TPC gas, has three shell structures: K, L, and M. The energy levels are 3.20 keV, 248 eV, and 16 - 52 eV, respectively. Since the collision probability with an electron is roughly proportional to its energy level, the lower energy-level excitations give a narrower dE/dx distribution.

4.2 dE/dx measurement

4.2.1 Derivation of the energy loss

The energy loss was measured using wire signals of the TPC. First, the wire signal clusters were searched in the z direction in the same way as the pad clusters. The pulse height of a cluster was determined from the peak amplitude of a parabola fitted to the highest 3 CCD buckets in the cluster. The z position of the cluster was also determined from the fit. The cluster was then associated to a track using the z information. If the cluster was within 1 cm of the track in the z direction, and not associated to other tracks, the cluster was linked.

The pulse-height amplitude was converted into the energy-loss value by two steps. The first was a correction for any non-linearity of the electronics. The second was a correction for the wire-to-wire gain variation. Details concerning the calibration are described in the following subsection.

Since a TPC sector has 175 sense wires, the energy loss for a track was sampled every 4-mm segment up to 175 independent data. A single variable, which is similar to the most probable energy loss, was deduced from the data sample. The final dE/dx was then derived by making various corrections, which are discussed later.

4.2.2 Calibrations

Prior to the experiment, after the electronics were calibrated by pulsing the shielding grid wires with various test-pulse amplitudes, the calibration curve for each channel was determined. The linearity of our electronics is better than 0.5% below the saturation point. The remaining non-linearity, appreciable near to the saturation point, is corrected using this calibration curve.

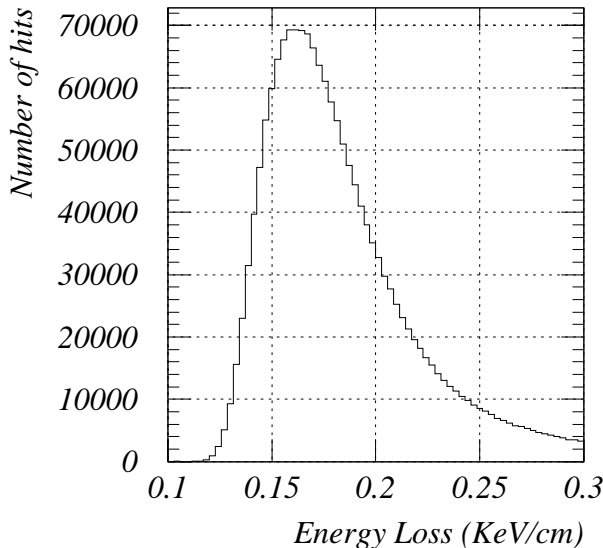


Figure 3: Pulse-height distribution obtained by the TPC wire signals for minimum ionizing pions.

After an electronics calibration, a correction for the wire-to-wire gain variation is made. Each sector is equipped with three rods having a ^{55}Fe X-ray source for each wire. Each rod can be moved pneumatically behind the hole on the cathode plane to irradiate wires. The wire-to-wire gain variation is corrected by calibrating the pulse height for the main peak of 5.9 keV for each wire. This calibration reduces the gain variation over a sector within a 3% level, and also gives the factor necessary to obtain the absolute value of the measured dE/dx .

4.2.3 The 65%-truncated mean

Figure 3 shows the measured energy-loss distribution in the TPC for minimum ionizing pions. The shape is asymmetric and has the long tail at the higher side. Therefore, a simple mean of the dE/dx sample for a track is not a good parameter for particle identification. The most probable energy loss or the mean value around the peak is a better parameter. We adapted the mean of the lowest 65% in the data sample (the 65%-truncated mean) as an estimator for the energy loss of a track. In the following we use dE/dx as in this meaning.

4.2.4 Corrections

To achieve a good resolution in dE/dx measurements, one must reduce the systematic shifts of the gain. In this section we discuss the systematic shifts of dE/dx and how we correct them.

In the TPC, measuring the energy loss is an indirect process. An implicit assumption is that the number of ionization electrons produced per track length is proportional to dE/dx of the charged particle. As electrons in the gas drift to the sectors they diffuse; some fraction is absorbed by impurities, such as O_2 , in the gas. Since the maximum drift length is more than 1 m, this effect is not negligible. We determined the attenuation factor using minimum ionizing pions in the momentum range between 0.5 and 0.6 GeV/c. Figure 4 shows the measured value of dE/dx as a function of the drift length. We correct this effect using following function:

$$PH_{correct} = PH_{measured} \times (1 + C_1 L),$$

where

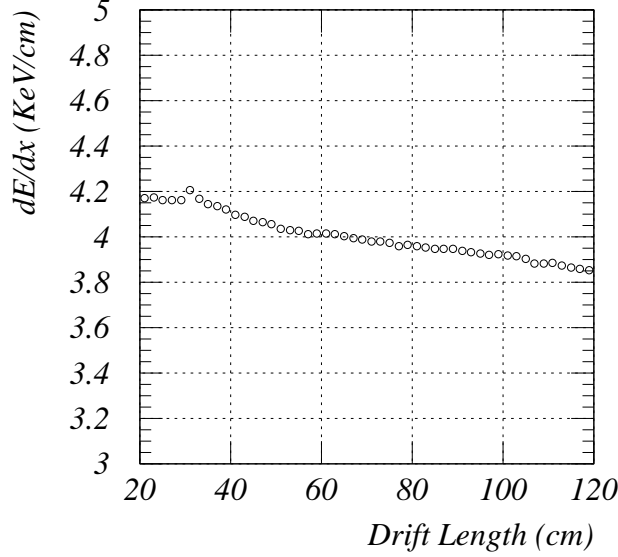


Figure 4: dE/dx as a function of the drift length.

PH is the pulse height, and

L is the drift length.

The attenuation factor (C_1) is typically 7% per meter.

The gain shift due to the sample thickness dependence was also corrected using the minimum ionizing pions. Figure 5 shows dE/dx vs. the path length on the logarithm scale. This systematic was corrected using

$$PH_{correct} = PH_{measured} \times (1 - C_2 \times \log(X)),$$

where

X is the path length normalized by 4 mm.

The factor C_2 was determined to be 0.2.

The electric fields near to the sense wires also affect the avalanche process. The dependence of the pulse height on the high voltage was parametrized as

$$PH_{correct} = PH_{measured} \times \left(1 - C_3 \times \frac{\delta V}{V_0}\right),$$

where

V_0 is the nominal high voltage (1970V) on the sense wire, and

δV is the variation of the voltage.

The correction factor (C_3) of the pulse height was determined using data taken in low high-voltage cosmic-ray runs. A 1% high-voltage change corresponds to a 17% change in the gain.

The electrons approaching the sense wires pass through the avalanche process. As the gas density increases the mean-free path of electrons becomes shorter and the soft collisions in which the electrons do not ionize the atoms increase; hence, the amplification factor drops. The gas density is proportional to the pressure and inversely proportional to the temperature. The pressure was well controlled, and its

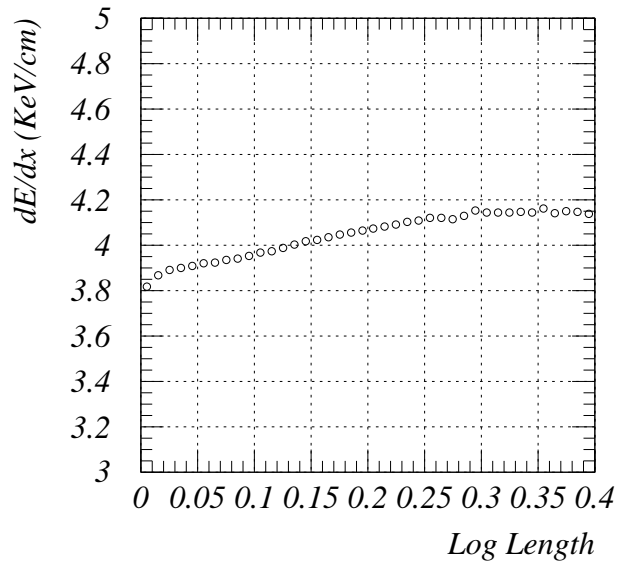


Figure 5: dE/dx as a function of the sample thickness in logarithm after a segment-length correction.

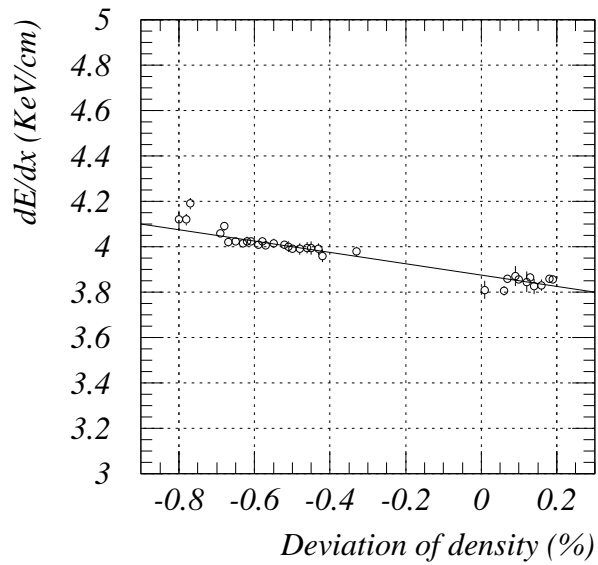


Figure 6: dE/dx as a function of the density from the nominal value.

variation was less than 0.04% throughout this experiment. The temperature of the gas was increased by about 2°C during the summer. Figure 6 shows dE/dx vs. the variation in the gas density. From the temperature change, we found that

$$PH_{correct} = PH_{measured} \times \left(1 + C_4 \times \frac{\delta\rho}{\rho_0}\right),$$

where

ρ_0 is the nominal gas density, and

$\delta\rho$ is the variation of the gas density.

The C_4 value was 6.0. A 1°C temperature change corresponds to about a 2% change in the gain.

After these corrections, we again carried out a wire-to-wire gain calibration. The event sample with minimum ionization pions were used for this purpose. After the pulse-height distributions for each wire were made and the correction factors were derived, a run-dependent correction was carried out. There were still unknown factors which changed the energy-loss values. Each step used a single run corresponding to a few 1000 beam events.

Finally, we derived the dE/dx distribution for momentum between 0.5 and 0.6 GeV, which was the minimum ionizing pion region. There were two peaks corresponding to pions and electrons. For several reasons, the relationship between these two peak values changed nonlinearly. One reason was an over-value setting of the threshold values in the electronics during some experiments. The other was a selection bias in the event pre-selection code in order to reduce the data size, mainly due to the vacuum condition. These caused a nonlinear offset in the pion dE/dx value. We thus corrected these by normalizing them to the initial experimental values in which the threshold values were considered to be sufficiently low. Furthermore, we fitted the width of two dE/dx peaks using the common ratio to the center values of the peaks using two Gaussians. The fitted width was considered to be the effect of this nonlinearity; the χ^2 s calculation is described later.

4.2.5 Velocity dependence of dE/dx

The dE/dx curve as a function of the particle velocity was determined from the data. Although theoretical calculations of the dE/dx curve reproduce the data fairly well, they are not adequate for particle-identification purposes, especially in the relativistic rise region. The data used for the determination were those from protons for the small- β region, cosmic-ray muons and minimum ionizing pions for low $\beta\gamma$, and electrons for the relativistic rise region. The data are fitted to a ninth-order polynomial parametrized as

$$\frac{dE}{dx} = \frac{1 + (\beta\gamma)^2}{(\beta\gamma)^2} \sum_{i=0}^9 c_i \left(\frac{\ln(\beta\gamma) - 4}{5}\right)^i - 0.70659,$$

where the c_i are given in Table 2. Figure 7 shows the dE/dx vs. momentum for tracks in more-than-three-track events. The bands of electrons, pions, kaons and protons can be clearly seen.

4.2.6 dE/dx resolution

The resolution of dE/dx was studied using the minimum ionizing pions. Figure 8 shows the dE/dx distribution of pions with momenta between 0.5 and 0.6 GeV/c. The resolution was estimated by fitting a Gaussian function to the distribution, and was obtained as $\sigma_{dE/dx} = 4.6\%$. The resolution for Bhabha events was also measured as $\sigma_{dE/dx} = 4.4\%$.

coefficient	value
c_0	6.2133
c_1	2.1340
c_2	-1.6116
c_3	-0.19783
c_4	0.0363802
c_5	-0.35785
c_6	1.4957
c_7	-0.16234
c_8	-0.95077
c_9	0.379

Table 2: Coefficients of the 9'th-order polynomial function.

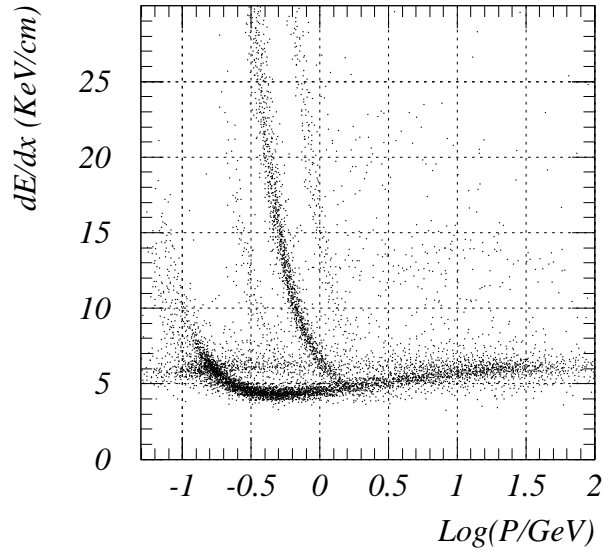


Figure 7: dE/dx vs. momentum for tracks in more-than-one-track events.

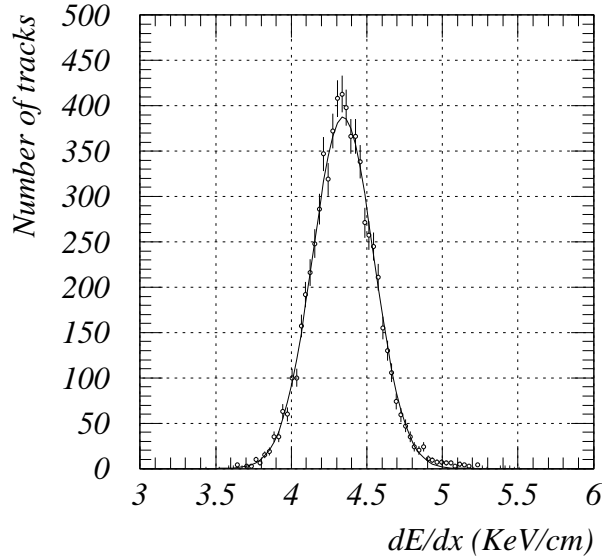


Figure 8: dE/dx distribution for minimum ionizing pions.

5 Energy measurement in the BCL

5.1 Clustering

The electromagnetic clusters detected with the BCL were used for electron identification. The method for electromagnetic energy clustering is described as follows:

1. We searched the maximum energy counter among 8 neighboring counters (at the +z or -z edge of the BCL, 5 counters) for counter by counter;
2. If the neighboring maximum counter energy was higher than its energy, the counter was merged to the neighboring one;
3. After the above procedures were iterated, the clusters were formed;
4. The cluster energy was calculated by summing the total counter energy in the cluster;
5. The azimuth angle (ϕ) and the z-position were calculated using the energy-weighted mean of the counter positions;
6. The depth of the cluster center was calculated according to $X = \ln(E/E_c) + 1.5$ (radiation length), where E is the cluster energy and E_c (12.6 MeV) is the critical energy of the BCL (lead glass);
7. The radial position (R) of the cluster was calculated according to the formula $R = R_{BCL} + X_0 \cdot X \cos \theta$, where R_{BCL} and X_0 are the inner radius and the unit radiation length of the BCL, i.e. 176cm and 1.7cm, respectively. Here, θ was assumed to be that of the maximum energy counter in the cluster, at first;
8. From z and this R, the θ was re-calculated; and
9. R and θ calculations were iterated two times.

5.2 Energy calibration

The monitoring system for the gains of 4300 counters comprises just one light source and an optical-fiber system. As the light source, a xenon flash lamp having a 3mm gap was chosen, because the emission spectrum resembles Čerenkov light. The amount of light received at a counter corresponds to about 7 GeV in energy. In order to correct for any variation in the light intensity of the xenon flash lamp, reference counters were placed in a temperature-controlled box. At each reference counter a NaI(Tl)- ^{241}Am light pulser was attached to measure the gain independently. The gain variation can be corrected to the 0.5% level.

The gain of each counter was calibrated with 4, 2, and 1 GeV electron beams from the IT1 beam line [12] at the 8-GeV Accumulator Ring (AR) at KEK.

We have accumulated Bhabha scattering events, after standard cuts of requiring two clusters of deposited energy greater than 1/3 of the beam energy at $|\cos\theta| < 0.77$ satisfying an acolinearity angle being less than 10° . The obtained resolution was 4.5%, apparently dominated by the nonuniformity in the gains of individual counters. The angular resolution was obtained to be 0.36° . Calibration of the individual counters was carried out using these Bhabha events. However, not all of the counters have been calibrated yet, due to a lack of statistics.

The electron energy-loss in the material in front of the BCL was investigated by studying the E/P for electrons. In this study we used an experimental two-track sample selected by the following criteria, expecting these to be dominantly $e^+e^- \rightarrow e^+e^-e^+e^-$ events:

1. The number of charged tracks with $P_T > 0.15$ GeV, the polar angle $|\cos\theta| < 0.83$, and the number of degrees of freedom (N.D.F.) of charged-track fitting ≥ 3 had to be 2;
2. The number of the BCL clusters with $E_{cluster} > 100$ MeV had to be at least 1; and
3. The visible energy (E_{vis}) of the event had to satisfy $E_{vis} < 30$ GeV, where both the charged tracks in the TPC and the clusters in the BCL were used.

Most of the selected events were expected to be two-photon events of $(e^+e^-)e^+e^-$, $(e^+e^-)\mu^+\mu^-$, and $(e^+e^-)\pi^+\pi^-$. The remaining ones were $\mu^+\mu^-$, $\tau^+\tau^-$, $e^+e^-\gamma$, etc. The used data corresponded to an integrated luminosity of 24.5 pb^{-1} at $\sqrt{s} = 50 \sim 60.8$ GeV. These selection cuts left 9120 two-track events.

To separate electron tracks from muons and pions, we used energy-loss (dE/dx) information from the TPC and TOF as follows: (1) The electron-candidate tracks were required to have dE/dx in the range of $5.5 \leq dE/dx \leq 7.5$ keV/cm; (2) the confidence level (CL) for the electron hypothesis by the TOF information had to be > 0.01 . We then calculated the E/P ratio of the energy measured by the BCL and the momentum measured by the TPC. The TPC-BCL combination was chosen when the distance between the BCL cluster and the extrapolated track was shortest. We only calculated the E/P for the TPC-BCL combination whose distance was less than 10cm.

To determine the BCL energy correction we fitted the E/P distribution with a second-order polynomial of the BCL energy. We used electron candidates which were in the energy range $E < 4.0$ GeV and the polar angle range $|\cos\theta| \leq 0.77$. The E/P-versus-energy distribution with the fitting curve is shown in Figure 9. Since real electrons should concentrate on E/P = 1, we obtained the following expression from the fitting result:

$$\begin{aligned} \frac{\Delta E}{E} &= 0.430 - 0.354 \cdot E + 0.072 \cdot E^2 \quad \text{for } E \leq 2.3\text{GeV, and} \\ &= 0 \quad \text{for } E > 2.3\text{GeV.} \end{aligned}$$

The E/P distributions in the momentum range $0.4 \leq P \leq 4.0$ GeV, E/P and momentum scatter plots with and without the BCL correction are shown in Figure 10.

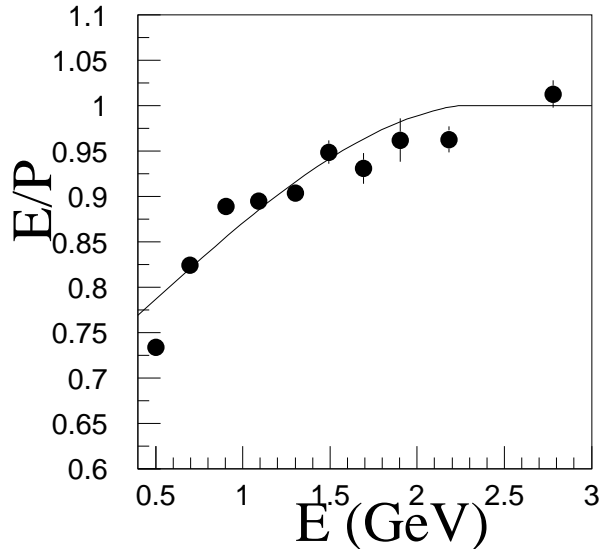


Figure 9: E/P ratio as a function of the BCL energy (filled circle). The solid line was obtained from a polynomial fitting (described in the text).

6 Detector simulation

6.1 Event generation

For single-photon-exchange process, we used JETSET6.3 as an event generator [13]. The parameters used in this program were fitted for general event shapes [14]. For two-photon processes, we used own event generator of which the details were described in reference [3, 15, 16].

6.2 Monte-Carlo simulation

The particles generated by the above-mentioned event-generation program were traced through the TOPAZ detector simulator. This detector simulation was designed to take into account all conceivable interactions which the particles might experience in the detector, and to mimic the detector response to them as closely as possible. The structures and materials of the detectors are precisely coded in the program and each particle is propagated by a small step from the interaction point. At each step, such interactions as decays, multiple scatterings, and bremsstrahlungs take place according to the probabilities associated with them.

In the TPC region the averaged energy loss in the gas is calculated according to a formula determined from the minimum ionizing pions in real data, knowing the velocity and charge of the particle. The Landau fluctuation is taken into account by smearing the energy loss so as to be consistent with the experimental distribution. The smeared energy loss is translated to a pulse height on the corresponding wire to be sampled in order to mimic the digitized outputs. Because the time profile of the wire signal was experimentally found to be independent of the track angle, a single pulse-height shape function is used to calculate the pulse height in each time bucket. The pulse height is digitized if it is above the threshold, and is recorded as wire data. Pad signals are generated using the pulse heights of the relevant five wires near to the pad rows. The avalanches on the five wires induced a charge along the pad row. We assume that the induced charge is a Gaussian distribution, and is proportional to the corresponding wire pulse heights. The width of the Gaussian and the weight factors for the five wires are determined experimentally [17].

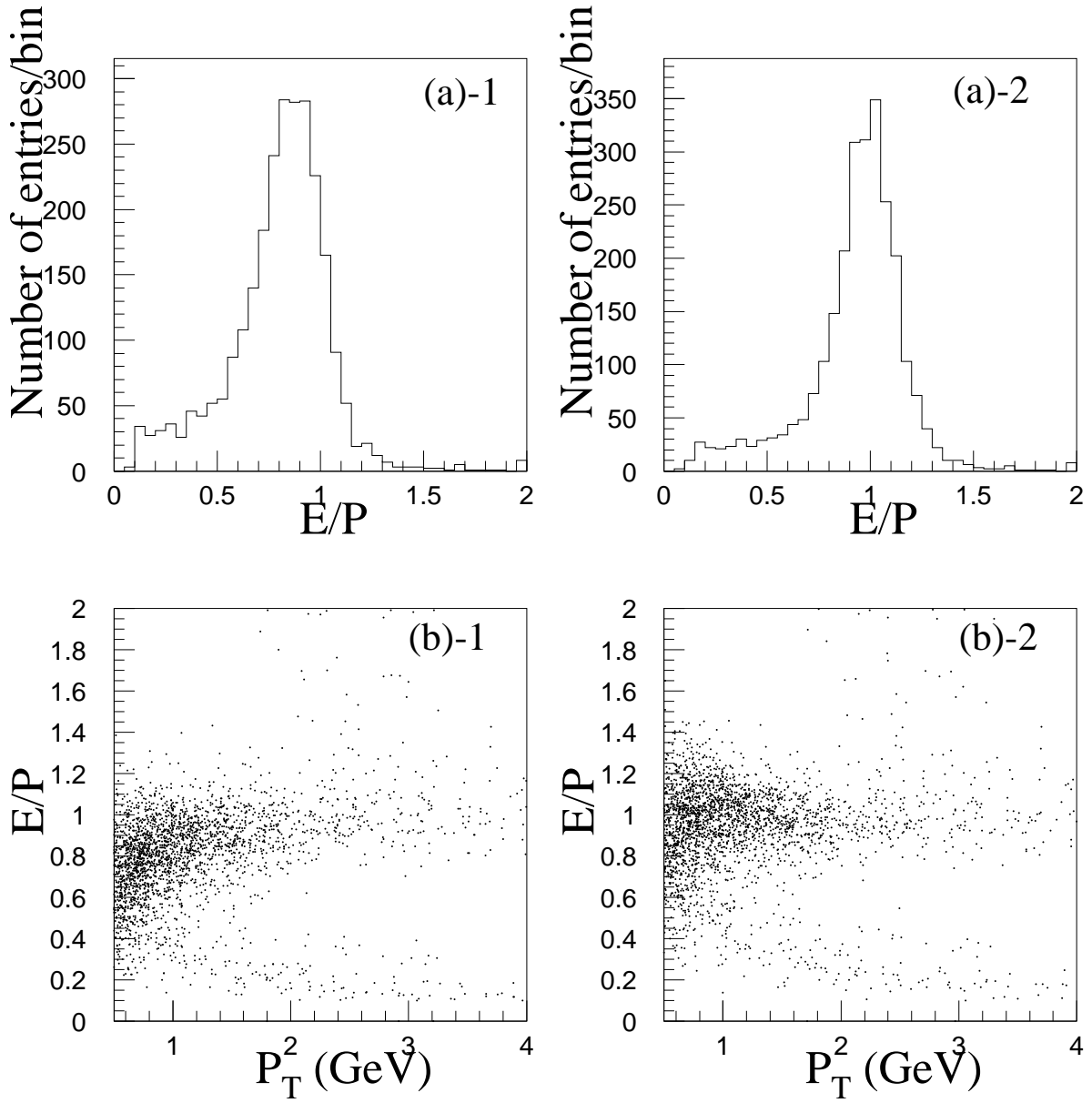


Figure 10: E/P distributions in the momentum range $0.4 \leq P \leq 4.0$ GeV [(a)-1 and 2] and Scatter plots of E/P vs. energy [(b)-1 and 2]. Indices 1 and 2 denote that without and with the BCL correction, respectively. The equation of the correction function is given in the text.

To simulate the electromagnetic shower development in the material, the EGS code is widely used [18]. The cut-off energy in the EGS program, when it is used, must be set at a value sufficiently lower than a critical energy for an accurate simulation, which consequently needs more CPU time. In the BCL, the electromagnetic shower is simulated by using the Bootstrap method to save CPU time [19]. This method utilizes pre-generated showers to obtain the shower density in cells of suitable size in the calorimeter. The development of a shower with an energy lower than the cut-off is replaced by them. Thus, once many sets of the frozen showers are prepared for various energies, the shower simulation can be carried out as accurately as that of the EGS code, while at the same time considerably reducing the CPU time.

For a nuclear interaction GEISHA 7 is used [20]. Short-lived particles such as K_s , π^0 , and Λ are decayed in the simulator program while keeping secondary vertex information.

7 Hadronic-event sample

7.1 Trigger

The charged trigger required at least two charged tracks with $P_T > 0.3-0.7$ GeV and an opening angle $> 45-70^\circ$, depending on the beam conditions. The neutral energy trigger required that the energy deposit in the BCL had to be greater than 2-4 GeV, or that in the ECL had to be greater than 10 GeV. Details concerning the trigger system can be found in reference [9].

7.2 Single-photon-exchange process

Our selection criteria for the single-photon-exchange process are as follows: (1) the number of good tracks had to be ≥ 5 , where a good track was required to have (i) a transverse momentum to the beam axis larger than 150 MeV, (ii) a distance of closest approach to the beam axis less than 5cm in the xy-plane, as well as in the z-direction, and (iii) a polar angle satisfying $0.02 \leq |\cos \theta| \leq 0.77$ to be well contained in the detector; (2) the visible energy (E_{vis}) had to be \geq the beam energy (E_{beam}), where E_{vis} is the sum of the momenta of the good tracks and the energies of BCL and ECL clusters of energy greater than 100 MeV; (3) the longitudinal momentum balance had to be $|\Sigma P_z|/E_{beam} \leq 0.4$, where the P_z 's were longitudinal momenta of the good tracks or longitudinal energies of the BCL and ECL clusters; (4) the larger of the hemisphere-invariant masses had to be greater than 2.5 GeV, where the two hemispheres were divided by a plane perpendicular to the thrust axis; and (5) those events with two or more large energy clusters of greater than $0.5E_{beam}$ were discarded. In total, 23,783 hadronic events were obtained. The corresponding luminosity was 197 pb^{-1} and the average center-of-mass energy was 58 GeV. The details can be found in reference [2, 21].

7.3 Two-photon process

The hadronic events produced by two-photon processes were selected based on the following criteria: (1) The number of good tracks had to be at least 4, where $|\cos \theta|$ should be less than 0.83; (2) the position of the origin of the event (i.e., the event vertex), reconstructed from all tracks, had to be within 1.5cm in the xy-plane and within ± 2.0 cm in z-direction; (3) E_{vis} had to be less than 30GeV, where only the BCL clusters were used for neutral energy; (4) the mass of the hadronic system (W_{vis}) had to be greater than 3GeV; and (5) the energy of the most energetic cluster appearing in the BCL, ECL, and FCL had to be less than $0.4E_{beam}$ (anti-tag condition). These selection cuts left 23,779 events at an integrated luminosity of 95.3 pb^{-1} . The average center-of-mass energy was 58 GeV. The details can be found in reference [3].

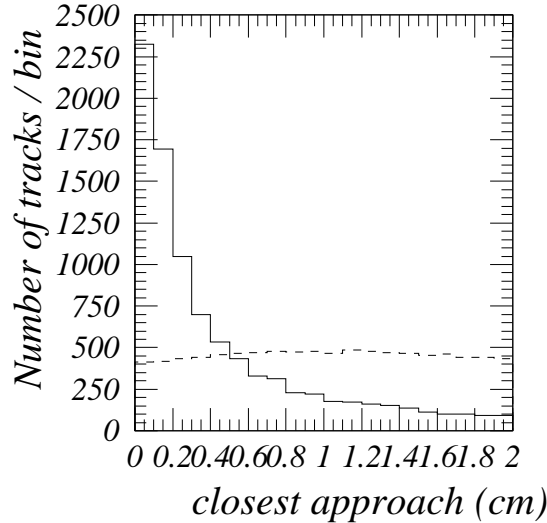


Figure 11: Distributions of the closest approach in the Monte-Carlo simulation; the solid histogram is for prompt electrons and the dashed one is for pair conversion and Dalitz decays.

8 Electron selection for a single-photon exchange

8.1 Good track selection

The electron tracks which satisfied good-track criteria were selected by the dE/dx information from the TPC and the E/P ratio measured with the TPC and BCL in a broad momentum region.

The selection criteria for good tracks were followings:

1. The closest approach to the beam axis in the xy-plane must be less than 1.0cm;
2. The closest approach to the interaction point in the z-direction must be less than 4.0cm;
3. The absolute value of the $\cos\theta$ of the track must be within between 0.02 and 0.83, where θ is the polar angle of the tracks with respect to the initial electron direction;
4. The transverse momentum with respect to the beam axis must be greater than 0.15 GeV/c;
5. The number of degrees of freedom (N.D.F.) of the track fitting must be greater than 3, with a maximum of 15;
6. The number of wires for the dE/dx calculation (65-% truncated mean) must be greater than 30, with a maximum of 114; and
7. The momentum must be greater than 0.8 GeV/c.

Conditions (1),(2), and (5) require good measurements of the momentum of the tracks. (1) also reduces the background. Condition (3) requires the tracks to be within the TPC active volume. (4) requires that the tracks are not curled up in the TPC volume. (6) is the condition for the sufficient resolution of dE/dx . (7) is added to reduce the background.

Figure 11 shows the difference of the closest approach to the beam axis in the xy-plane for prompt electrons and the background tracks in a Monte-Carlo simulation. Figure 12 shows the difference in the momentum distribution for prompt electrons and the background tracks in a Monte-Carlo simulation.

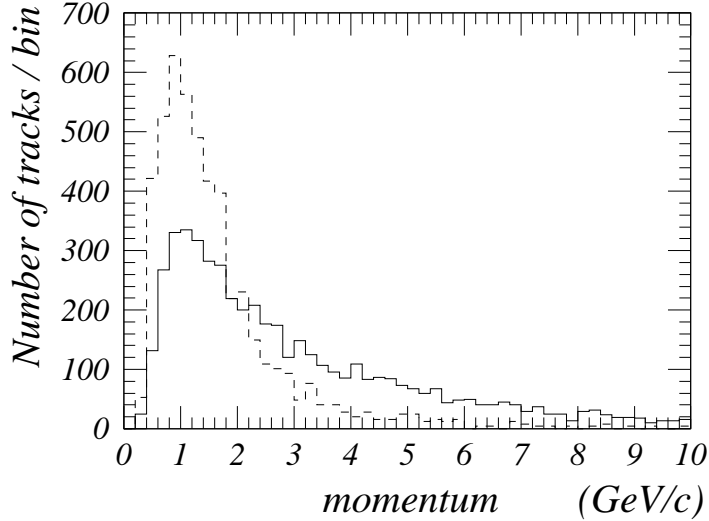


Figure 12: Distributions of the momentum in the Monte-Carlo simulation; the solid histogram is for prompt electrons and the dashed one is for the background.

After the tracks were subsequently extrapolated to the radius of each BCL cluster center, we calculated the distance to the clusters. The cluster was matched with the track having the closest distance. E/P was calculated using a matched track and cluster.

8.2 Electron selection

The electron selection was carried out based on two criteria.

First, we calculated the χ_i^2 s for each hypothetical particle using a dE/dx information and a momentum measurement from the TPC, where i indicates an electron, muon, pion, kaon, or proton. The definition of χ_i^2 is

$$\chi_i^2 = \left(\frac{\frac{dE}{dx}_{meas.} - \frac{dE}{dx}(\beta\gamma)}{\Delta \frac{dE}{dx}_{meas.}} \right)^2 + \left(\frac{\beta\gamma_{meas.}^i - \beta\gamma}{\Delta(\beta\gamma)_{meas.}} \right)^2,$$

with

$$\beta\gamma_{meas.}^i = \frac{P_{meas.}}{M_i}.$$

Here, $\Delta \frac{dE}{dx}_{meas.}$ and $\Delta(\beta\gamma)_{meas.}$ are the estimated errors of $\frac{dE}{dx}_{meas.}$ and $\beta\gamma_{meas.}^i$, respectively. They include inefficiency measurements in the TPC. $\Delta \frac{dE}{dx}_{meas.}$ also includes the effect of the nonlinear shift described before. The most probably χ_i^2 is given by minimizing it while modifying $\beta\gamma$. The expected dE/dx is given by a polynomial function of $\beta\gamma$. The details are described in Section 4.2.5.

The electron-candidate tracks were selected by requiring that χ_e^2 must be less than 3.0, where the number of degrees of freedom (N.D.F.) is 1. Figure 13 shows the E/P distributions both before and after this selection. The peak of the electrons is enhanced.

The rejected tracks in this selection (dE/dx -hadron) are used for hadron background estimations.

Second, we required the electron-candidate tracks to have a distance of less than 5.0cm with respect to the calorimeter cluster positions, and calculated the cluster width, which is the energy-weighted r.m.s. of counter positions with respect to the extrapolated track position. We also carried out selection for

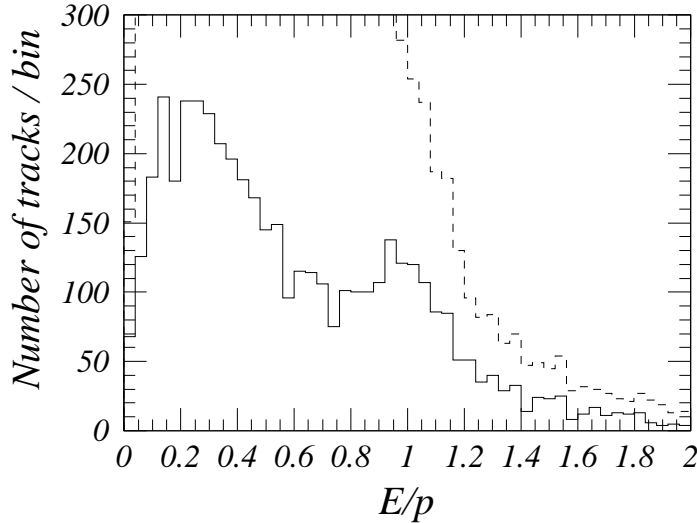


Figure 13: E/P distribution of the experimental data; the dashed histogram is for the before dE/dx selection and the solid one is for the after dE/dx selection.

the cluster width, i.e., we selected the clusters having widths of between 1.0cm and 10.0cm. These distributions for electron-candidate tracks and hadron tracks are shown in Figure 14.

The E/P distributions of before and after these selections are shown in Figure 15.

8.3 Background estimation

8.3.1 γ -conversion rejection

Since the largest background source was electrons from γ -conversions at the material in front of the TPC, we rejected the dominant part of such electrons by the following methods.

We reconstructed secondary vertices (V^0 's) with an electron-candidate track and one of the unlike sign charged tracks, and then calculated the invariant mass of each V^0 , assuming that its daughter particles are electrons. For the V^0 -reconstruction, two kinds of vertices, i.e., non-crossing and crossing cases in the xy-plane (perpendicular to the beam axis), were searched. In the former case, the combinations with a distance in the xy-plane of less than 4.0cm and a z-distance of less than 2.0cm were selected; we required that the deflection angle between the momentum vector of two tracks and the position vector of the closest point be less than 5.0 degrees. In the latter case, we selected one vertex which had a smaller deflection angle, and required that the z-distance be less than 2.0cm and the deflection angle be less than 5.0 degrees.

We then rejected the tracks in the pair if its invariant mass was ≤ 50 MeV in the former or ≤ 200 MeV in the latter cases, respectively.

These distributions are shown in Figure 16.

8.3.2 Hadron background estimation

The hadron background on the E/P plot was estimated using the dE/dx -hadrons. The distributions were normalized using the entries between 0.0 and 0.64. The normalized E/P distributions of the dE/dx -hadrons were subtracted from the E/P distributions of the selected electron candidates. The numbers of

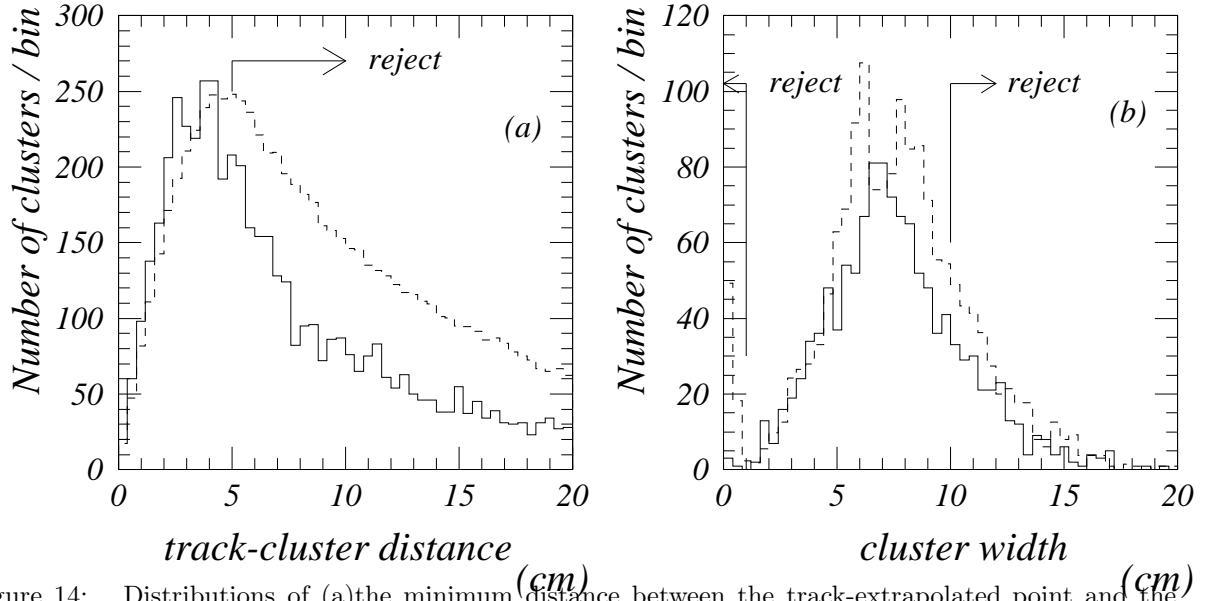


Figure 14: Distributions of (a) the minimum distance between the track-extrapolated point and the cluster, and (b) the shower width with respect to the track; the solid histograms and the dashed histograms are the total tracks and the electron-enhanced samples of the hadronic events, respectively.

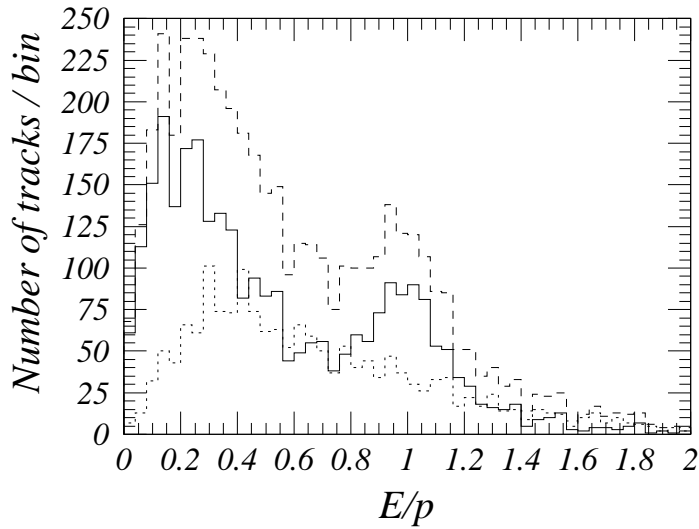


Figure 15: E/P distribution of the experimental data; the solid and the dashed histograms are after and before the shower selection, respectively. The dotted one is for the rejected tracks by this selection.

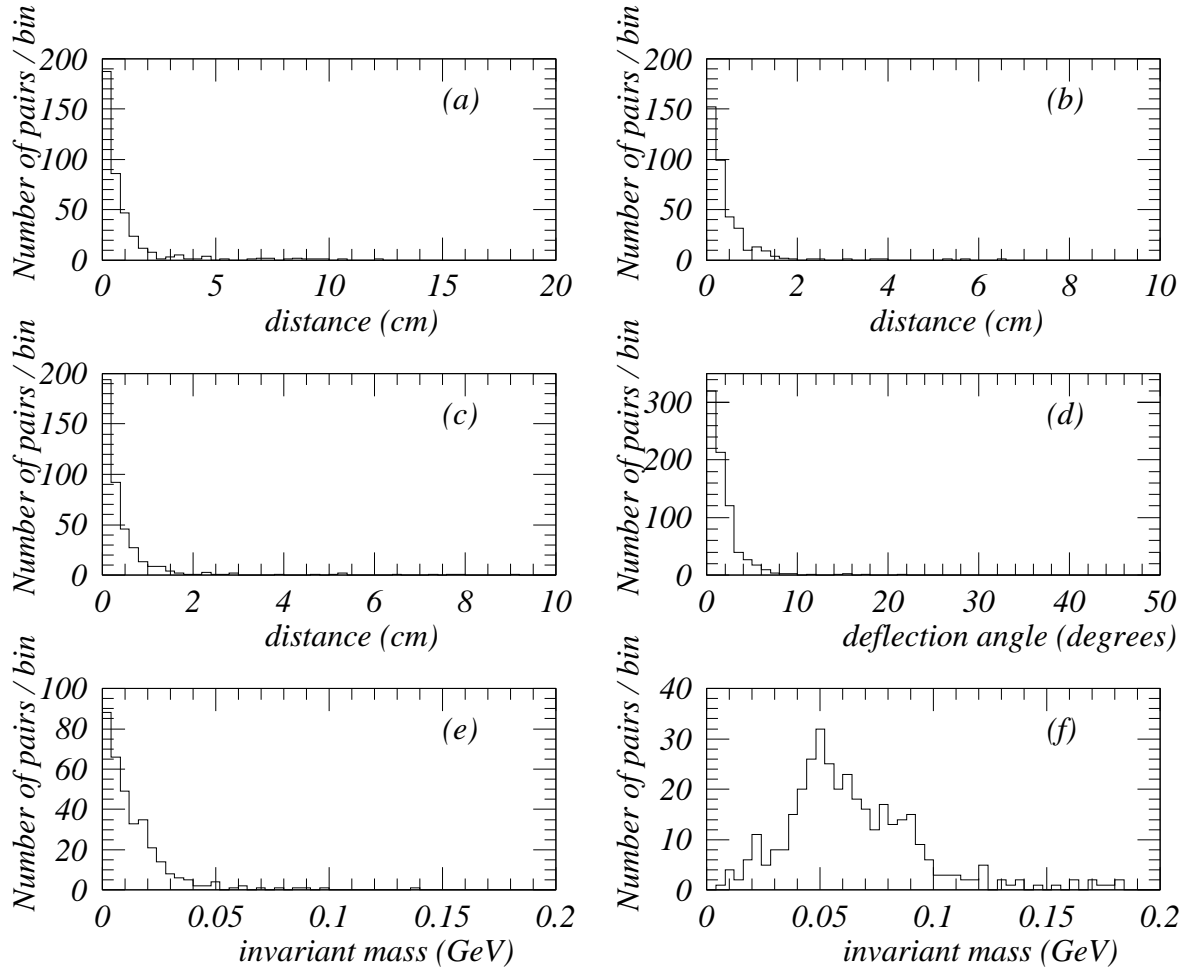


Figure 16: Distributions of the secondary vertices in the Monte-Carlo simulation; (a)the distance in the xy-plane of the not intersected case, (b)the distance in the z-direction of the not intersected case, (c)the distance in the z-direction of the intersected case, (d)the deflection angle of both cases, (e)the invariant mass of the not-intersected case, and (f)the invariant mass of the intersected case.

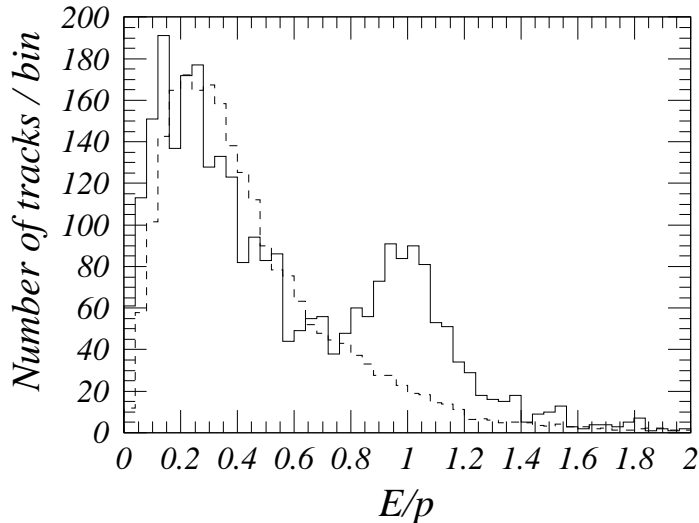


Figure 17: Example of the hadron background estimation; the solid and dashed histograms are the selected electron candidates and the dE/dx -hadrons which is described in the text, respectively.

electrons were obtained by counting the entries between 0.74 and 2.0 in the subtracted E/P distributions. An example of the hadron-background estimation is shown in Figure 17.

8.3.3 Remaining γ -conversion estimation

There remained electrons resulting from γ -conversions which escaped from V^0 reconstruction. They were presumably energy-unbalanced pairs, for each of which the lower P_T track was not reconstructed by the TPC. We estimated the failure rate of the V^0 reconstruction by a Monte-Carlo simulation. The failure rate, $\eta = N_{V^0 \text{ failure}}^{M.C.} / N_{V^0 \text{ reconstructed}}^{M.C.}$, was estimated for each P_T -bin. In the calculation, we included contributions from Dalitz decay ($\pi^0 \rightarrow e^+e^-\gamma$) as well as the conversion electron pairs. Since we did not apply any vertex position cut in the conversion-pair reconstruction, this factor included the effect on the Dalitz pairs. In order to estimate the number of remaining background tracks from γ -conversions, we multiplied the number of reconstructed conversion pairs in the experiment by η in each P_T bin.

8.4 Pion-rejection factor, electron efficiency

The electron selection in the single-photon-exchange process is summarized here. The pion-rejection factors were derived using single-track multi-hadron events generated by Monte-Carlo simulations. In order to derive the efficiency and the factor, we required E/P to be within 0.72 to 2.0 for the selected tracks. All of the tracks which passed the above criteria were counted. The definition of the selection efficiency is the ratio of the number of electrons counted (as above) to the number of charged tracks before all of the selection criteria. The pion-rejection factor is defined as the ratio of the number of pions before selection to the number of the remaining pions with an E/P of between 0.72 and 2.00.

This value for single-track events is shown in Figure 18, together with the electron efficiency. Since the dE/dx curve of the pions is close to that of the electrons at the higher momentum region, the pions satisfy the dE/dx selection criterion. Thus, the pion rejection factor is worse in the higher momentum region. The average values were 80 for pion rejection and 68.4% for electron efficiency. In order to extract these two averages, we assumed the momentum spectrum in the multi-hadron events.

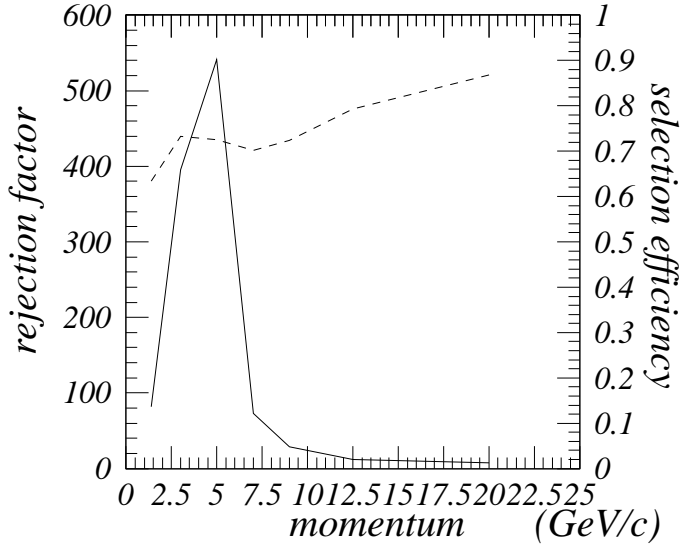


Figure 18: Pion-rejection factor and electron efficiency for single-track events; the solid curve is the pion-rejection factor (left scale) and the dashed one is the electron efficiency (right scale).

In practice, further rejection was carried out. The pions remaining after the E/P selection were estimated using the tracks rejected by the dE/dx selection (dE/dx -hadrons). The E/P distributions of the dE/dx -hadrons were normalized using the entries in the side-band ($0.0 < E/P < 0.64$); then the distribution from the E/P distribution of the selected tracks was subtracted. This procedure improves the pion rejection factor by more than factor 3.

For multi-hadron events, we show these values for two cases, i.e., low- P_T ($P_T < 0.8$ GeV) and high- P_T ($P_T > 0.8$ GeV). They are shown as a function of the electron momentum in Figures 19 and 20. The same E/P selection was carried out as that described above to derive these Figures. For the higher momentum tracks, the pion-rejection factors are rather worse because of the dE/dx effect (as described before). To summarize, the pion-rejection factors of high- P_T tracks and low- P_T tracks were estimated to be 164 and 137 on the average, where the electron efficiencies were 68.4 and 42.7%, respectively. Practically, we also used additional pion rejection by fitting (as mentioned above). We can thus expect better rejection of the pions.

9 Electron identification in two-photon processes

9.1 Electron selection

In two-photon processes electron tracks were identified by combining the information from the E/P ratio, dE/dx , and the TOF as follows:

1. Charged tracks in the TPC were extrapolated to the BCL. We then selected for each TPC track the BCL cluster which was the closest. The E/P of each of the so-selected TPC-BCL combinations had to satisfy $0.75 \leq E/P \leq 1.25$.
2. dE/dx was calculated for the electron-track candidate to be used in the subsequent electron counting. The resultant dE/dx was mostly contained in the range $5.5 \leq dE/dx \leq 7.5$ keV/cm.
3. We used information from the TOF and required the track to have a confidence level(CL) of 0.01 or better for the electron hypothesis.

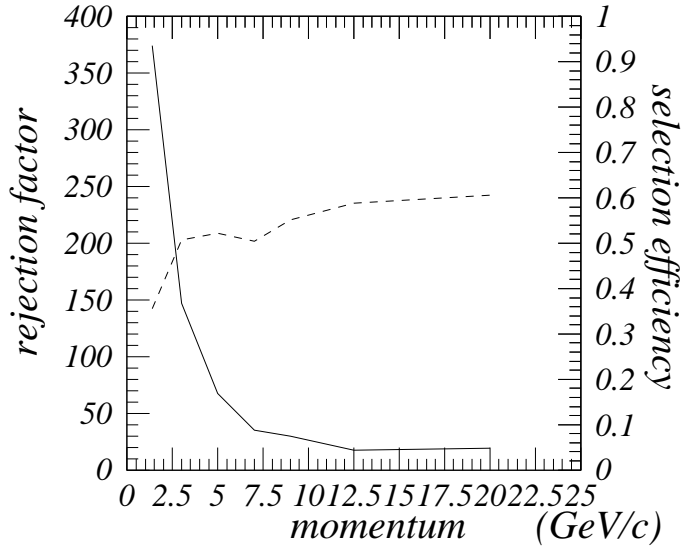


Figure 19: Pion-rejection factor and electron efficiency for low- P_T tracks; the solid curve is the pion-rejection factor (left scale) and the dashed one is the electron efficiency (right scale).

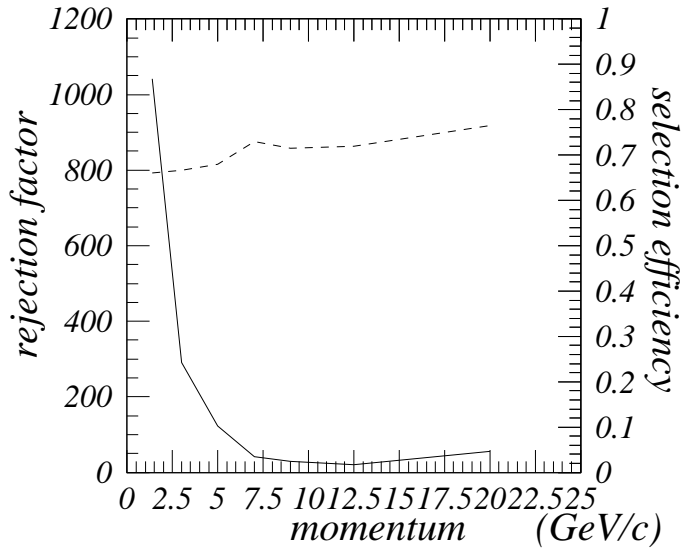


Figure 20: Pion-rejection factor and electron efficiency for high- P_T tracks; the solid curve is the pion-rejection factor (left scale) and the dashed one is the electron efficiency (right scale).

The energy-loss (dE/dx) information from the TPC enables us to separate electrons from hadrons in the momentum region ($P_T < 3\text{GeV}$). The E/P ratio of the energy (E) measured by the BCL and the momentum (P) measured by the TPC can separate electrons clearly above 0.4 GeV. The TOF was useful to resolve electrons from kaons and protons in the overlapping region of dE/dx .

The performance of electron identification in the momentum range $0.4 \leq P_T \leq 3.0$ GeV and the polar-angle range $|\cos\theta| \leq 0.77$ is demonstrated in Figures 21, where various distributions (the closest TPC-BCL distance (Figure 21-(a)), the E/P ratio (Figure 21-(b)), the CL for the electron hypothesis in the TOF (Figure 21-(c)), and the dE/dx (Figure 21-(d))) are shown. In these figures, electrons coming from γ -conversions were already rejected. The methods for γ -conversion rejection are described in the next section. Notice that these figures were obtained with the electron candidates selected by all of the cuts except for that on each plotted quantity. Notice in particular that Figures 21-(a) to (c) were made with an dE/dx cut ($5.5 \leq dE/dx \leq 7.5$ keV/cm) which was used only for the purpose of displaying. As can be seen from the dE/dx distribution in Figure 21-(d), two peaks corresponding to electrons and pions are clearly separated.

We counted the numbers of electrons in each P_T bin by fitting the dE/dx distributions with double Gaussians bin by bin. The P_T binning was selected so as to approximately equalize the number of entries in each bin. The dE/dx distributions are shown in Figures 22.

9.2 Reject γ -conversions

The electrons from the γ -conversions were rejected by secondary vertex (V^0) reconstruction. The V^0 's were reconstructed from all combinations of two tracks, and the invariant mass of each V^0 were calculated. When two tracks did not intersect at the closest point in the xy-plane, the distances of the two tracks at the minimum-distance position were required to be less than 7 cm in the xy-plane and 3 cm in the z-direction. When two tracks intersected, we chose from the two crossing points that with the shorter z-difference, and required it to be less than 1.5 cm. We then rejected the tracks in the pair if its invariant mass was ≤ 80 MeV in the former or ≤ 150 MeV in the latter cases.

We also required the closest approach of each electron-track candidate to the event vertex in the xy-plane to be < 0.5 - 1.5 cm, depending on P_T .

9.3 Remaining γ -conversion estimation

The remaining γ conversions and Dalitz decays were estimated using the failure rate of the V^0 reconstruction which was obtained by a Monte-Carlo simulation. The failure rate of the V^0 reconstructions (described in section 8.3.3) was estimated for each P_T -bin, and was typically ~ 0.4 . The number of remaining background tracks was estimated by this ratio multiplied by number of the reconstructed conversion pairs in the experiment in each P_T bin. The γ -conversion and Dalitz decay background mainly occupy the low- P_T region.

9.4 Pion rejection factor and electron efficiency

The electron selection in the two-photon processes is summarized here. The electron efficiencies for single-track events and for multi-hadron events which were generated by the Monte-Carlo simulation are shown in Figures 23 and 24, respectively, as a function of the transverse momentum of the track. The average values of the efficiencies were 34.2% for single-track events and 36.0% for multi-hadron events. The former value was obtained assuming the P_T distribution in the multi-hadron events.

The pion-rejection factors were also derived with single-track and multi-hadron events. For single-track events we obtained a pion-rejection factor of 15000 for the high momentum region of $1.5 \leq P_T \leq 3.0$ GeV where the factor was the smallest. The pion-rejection factor for multi-hadron events is indicated in Figure 24 by the dashed line. The average value for multi-hadron events was 8600. In the real analysis we

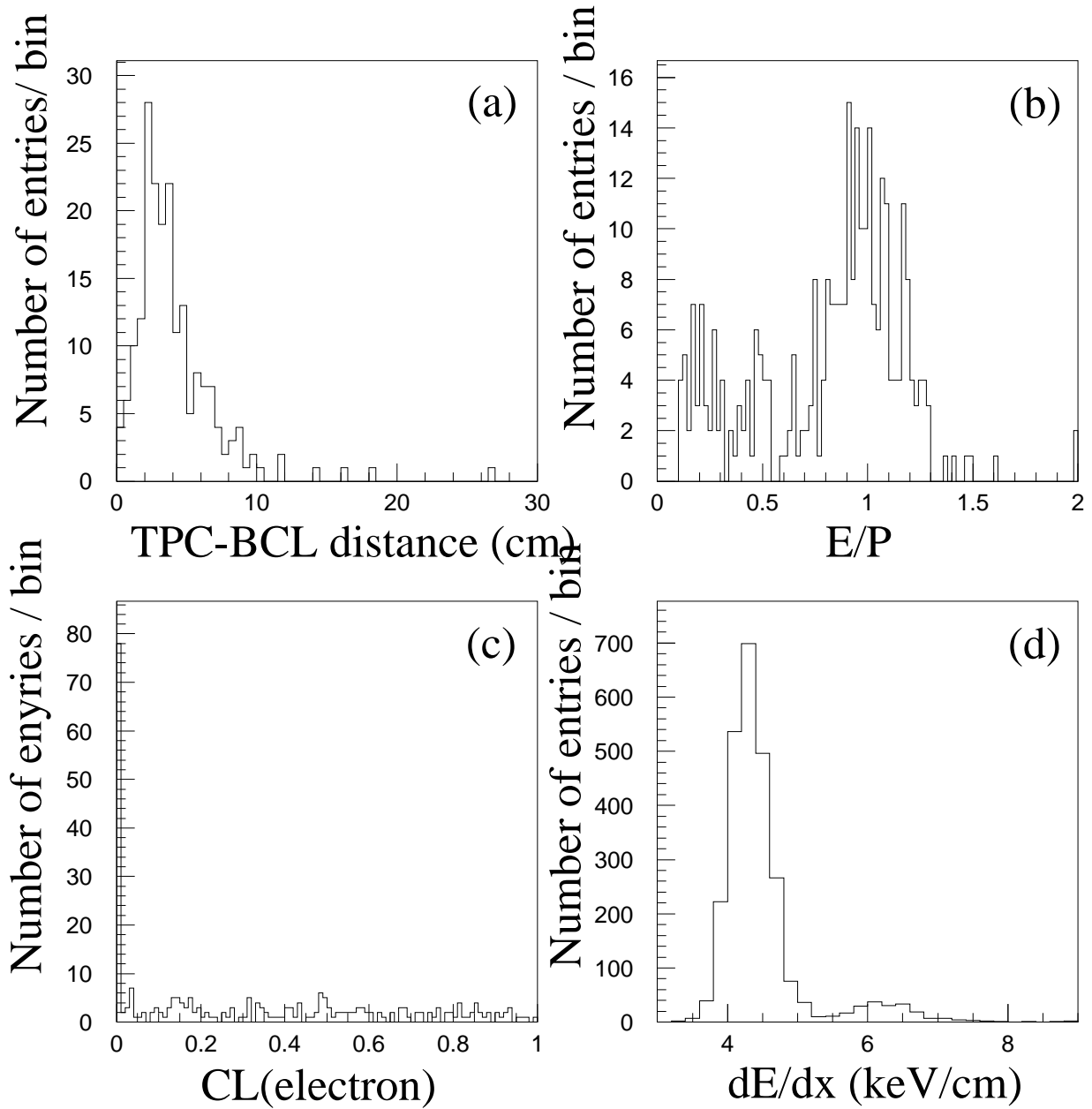


Figure 21: Various distributions for electron candidates: (a) the distance between a TPC track and its closest BCL cluster, (b) E/P, (c) the confidence level (CL) for the TOF, and (d) dE/dx . Each of these distributions was obtained with all of the cuts except for that on the plotted quantity.

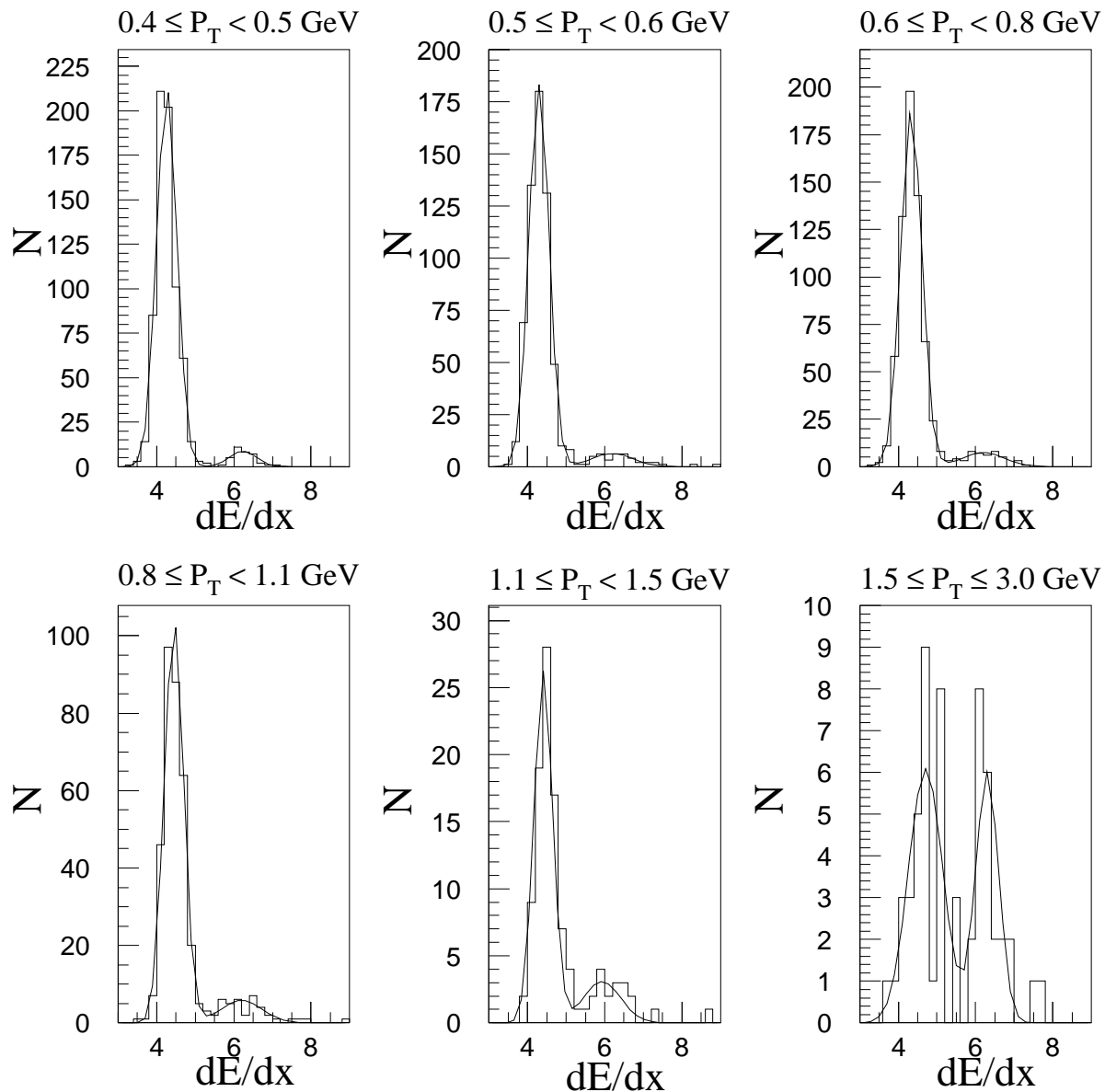


Figure 22: dE/dx distributions for each P_T -bin indicated in the figure. The smooth lines are the best-fit curves described in the text.

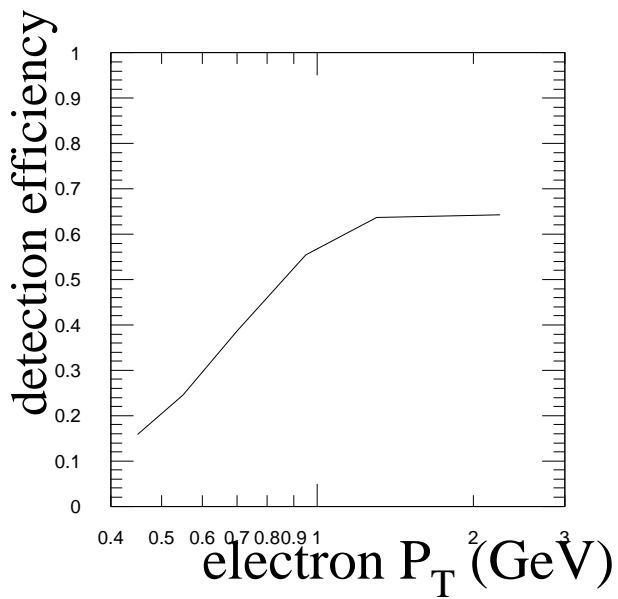


Figure 23: Detection efficiency of electron tracks for single-track events.

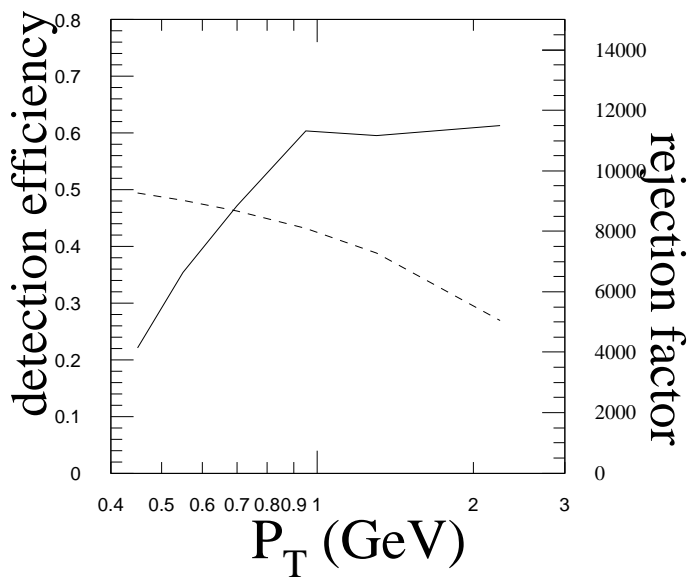


Figure 24: Pion-rejection factor and electron efficiency for two-photon hadronic events; the dashed curve is the pion-rejection factor (right scale) and the solid one is the electron efficiency (left scale).

counted the number of electrons by fitting the dE/dx distributions. Therefore, in fact, the pion-rejection factor was far better than these values.

10 Summary

We have developed a method to identify electrons inside hadronic jets using the time-projection chamber and the lead-glass calorimeter in the TOPAZ detector system at TRISTAN. The energy-loss measurement with the time-projection chamber and the energy measurement with the lead-glass calorimeter provided good electron identification over a wide momentum range. In particular, low- P_T ($P_T > 0.4$ GeV) electron identification was proven to be possible. This is powerful for studying the open-charm production in two-photon processes. The pion-rejection factors and the electron efficiencies inside hadronic jets were obtained to be 163 and 68.4% for high- P_T electrons and 137 and 42.7% for low- P_T electrons in single-photon-exchange process, and 8600 and 36.0% for two-photon processes.

Acknowledgement

We thank the members of the TOPAZ collaboration for their support and valuable discussions. Special thanks go to Drs. R. Itoh, K. Nagai, and T. Tauchi for the analysis and calibration for the time-projection chamber and the lead-glass calorimeter. We appreciate all of the engineers and technicians at KEK as well as the collaborating institutions. This work was partially supported by a Grant-in-Aid for Scientific Research from the Japan Ministry for Education, Science and Culture. One of us (E.N.) was supported by Japan Society for the Promotion of Science.

References

- [1] K. Nagai et al., Phys. Lett. **B 278** (1992) 506.
- [2] E. Nakano et al., Phys. Lett. **B 340** (1994) 135.
- [3] M. Iwasaki et al., KEK preprint 94-109, to be published in Phys. Lett. **B**.
- [4] M. Drees and K. Grassie, Z. Phys. **C 28** (1985) 451; H. Abramowicz, K. Charchula, and A. Levy, Phys. Lett. **B 269** (1991) 458.
- [5] M. Drees, M. Kämer, J. Zunft, and P. M. Zerwas, Phys. Lett. **B 306** (1993) 371.
- [6] T. Kamae et al., Nucl. Instrum. Meth., **A 252** (1986) 423.
- [7] S. Kawabata et al., Nucl. Instrum. Meth. **A 270** (1988) 419.
- [8] A. Imanishi et al., Nucl. Instrum. Meth., **A 269** (1988) 513; A. Yamamoto et al., Jpn. J. Appl. Phys. Lett., **25** (1986) 423; J. Fujimoto et al., Nucl. Instrum. Meth., **A 256** (1987) 449; S. Noguchi et al., Nucl. Instrum. Meth., **A 271** (1988) 464; H. Hayashii et al., Nucl. Instrum. Meth., **A 316** (1992) 202.
- [9] R. Enomoto et al., Nucl. Instrum. Meth., **A 269** (1988) 507; R. Enomoto, K. Tsukada, N. Ujiie, and A. Shirahashi, IEEE trans. NS. **Vol. 35, No. 1** (1988) 419; T. Tsukamoto, M. Yamauchi, and R. Enomoto, Nucl. Instrum. Meth. **A 297** (1990) 148.
- [10] K. Fujii et al., Nucl. Instrum. Meth., **A 264** (1988) 297.
- [11] A. Shirahashi et al., IEEE Trans. Nucl. Sci. **35** (1988) 414.

- [12] K. Ogawa et al., KEK internal Report, 85-2 (1985).
- [13] T. Sjöstrand and M. Bengtsson, *Comp. Phys. Comm.* **43** (1987) 367.
- [14] I. Adachi et al., *Phys. Lett.* **B 227** (1989) 495.
- [15] H. Hayashii et al., *Phys. Lett.* **B 314** (1993) 149.
- [16] R. Enomoto et al., *Phys. Lett.* **B 328** (1994) 535.
- [17] R. Itoh et al., *IEEE Trans. on Nucl. Sci.* **NS-34** (1987) 533.
- [18] W. Nelson, H. Hirayama, and D. Rogers, SLAC-Report-265 (1987), unpublished.
- [19] E. Longo and L. Luminari, *Nucl. Instrum. Meth.* **A 239** (1985) 506.
- [20] H. Fesefeldt, PITHA 85/02 (1985)
- [21] K. Miyabayashi et al., submitted for publication.